ELSEVIER

Optics and Lasers in Engineering 40 (2003) 353–369

OPTICS and LASERS in ENGINEERING

Dynamic fracture behavior of syntactic epoxy foams: optical measurements using coherent gradient sensing

Medhat A. El-Hadek, Hareesh V. Tippur*

Department of Mechanical Engineering, Auburn University, 202 Rose Hall, AL 36849, USA

Abstract

Dynamic fracture behavior of syntactic foams made of thin-walled microballoons dispersed in epoxy matrix is studied. Monotonically decreasing dynamic Young's modulus with increasing volume fraction of microballoons is observed using ultrasonic pulse-echo and density measurements. The results are also in good agreement with the Hashin–Shtrikman lower-bound predictions for elastic porous solids. Dynamic crack initiation toughness and crack growth behaviors are examined using instrumented drop-tower tests and optical measurements. Crack initiation toughness shows a linear relationship with Young's modulus over the entire range of volume fraction of microballoons studied. A proposed model based on simple extension of micromechanics prediction agrees well with the measurements. The optical method of coherent gradient sensing (CGS) has been used along with high-speed photography to record crack tip deformation histories in syntactic foam samples subjected to impact loading. Pre- and post-crack initiation events have been successfully captured and apparent dynamic stress intensity factor histories are extracted from the interferograms. Results suggest increasing crack speeds with volume fraction of microballoons. No significant dependence of dynamic fracture toughness on crack speed in any of the volume fractions is observed.

Keywords: Syntactic foam; Porosity; Dynamic fracture; Impact; Interferometry

1. Introduction

Syntactic foams can be distinguished from conventional foams in the way they are manufactured namely by mechanically blending thin-walled microballoons in

*Corresponding author.
E-mail address: htippur@eng.auburn.edu (H.V. Tippur).

0143-8166/03/$ - see front matter
PII: S0143-8166(02)00095-7

different polymeric or metallic matrix materials. Thus porosity in syntactic foams comes from the 'filler' which is typically hollow glass, ceramic or polymer microballoons. Further distinction is that the porosity in these materials is typically microscopic in nature and can be easily controlled. The range of engineering applications of syntactic foams have increased in recent years due to the manufacturing simplicity, specific strength, insulating and energy absorbing characteristics [1]. One of the most significant applications for syntactic foams is in the area of naval and undersea marine equipments [2–3], where it has been used as structural element for decks and submarines buoys. Syntactic foams are also used in civil and industrial engineering, as imitation wood and marble, because of the good shear stiffness and specific strength [4]. Due to the high specific energy absorption, and impact resistance [5], syntactic foams have been considered for army vehicles and for personnel protection. Syntactic foams made with glass and carbon microspheres are used in aerospace structures, missile heads and heat shields for space vehicles [6]. They are also employed in electronics and telecommunications due to superior thermal and dielectric properties [7]. The need for low cost, lightweight, bio-compatible materials has led to the exploration of porous syntactic materials for potential biological [8–9] applications.

Among the methods for mechanical characterization of foams, the ones developed by Gibson et al. [10] are widely used. They have introduced relations of the form $\Phi = C(\rho/\rho_s)^q$ for the mechanical properties, where Φ denotes the material property, ρ is the effective density, ρ_s is the density of the wall material, C and q are constants dependent on cell geometry determined either experimentally or analytically. In their later work, Maiti et al. [11] have introduced a semi-empirical relationship that shows fracture toughness of cellular materials relative to that for the wall material depends on the density ratio as well. Elastic characteristics of porous materials could also be determined using micromechanics models such as the ones proposed by Hashin and Shtrikman [12] and modified Mori–Tanaka approaches [13] for multiphase materials by setting the filler phase elastic properties to zero. Among other methods, Krstic and Erickson [14] have taken a linear elastic fracture mechanics approach for predicting Young's moduli of elastic porous solids wherein cylindrical and spherical pores are assumed to possess radial or annular flaws. Nielsen [15] has established relationships between Young's modulus and strength of porous materials for aiding non-destructive evaluation of porous materials. Recently, Rizzi et al. [16] have studied tensile and compressive behaviors of pre-fabricated syntactic foams of a particular volume fraction. Experimental measurement of elastic modulus, tensile strength and crack initiation toughness of epoxy and urethane syntactic foams have been reported by El-Hadek and Tippur [17]. They have also proposed and validated simple energy-based models for predicting their properties by treating them as porous materials. Fabrication and impact behaviors of syntactic foams have been studied by Kin and Oh [18].

As evident from the above, despite their potential application in a wide range of dynamic loading environments, investigation into the dynamic fracture behavior of syntactic foams is currently lacking. In this work, dynamic crack initiation and growth in syntactic epoxy foams is studied under low-velocity impact loading

conditions. Effect of volume fraction of the microballoons in the matrix on crack initiation and crack growth are examined. In the next section, preparation and elastic characterization of homogeneous epoxy syntactic foams of different volume fractions is described. Section 3 describes dynamic crack initiation toughness measurements along with micromechanics-based models for predicting the mechanical properties. Optical measurement of crack initiation and growth in different volume fractions are described in Section 4. The results are summarized in Section 5.

2. Material preparation and elastic characterization

Syntactic epoxy foam sheets with randomly distributed microballoons were prepared. The volume fraction, V_f, of the microballoons in these sheets ranged between 0 and 0.45. The microballoons used in this investigation were commercially available hollow soda-lime glass spheres of mean diameter of $\sim 60\,\mu m$ and wall thickness $\sim 400\,nm$. The extremely small (nano-scale) wall thickness relative to the diameter of these fillers makes the mixture behave like a porous material.

Two-part epoxy with relatively low viscosity, low shrinkage and long duration (72 h) curing characteristics was used as the matrix material. Elastic wave speed measurements using ultrasonic pulse-echo technique was used for ensuring homogeneity of the material. Some of the relevant physical and mechanical properties of the constituents are listed in Table 1.

The values of *dynamic* Young's moduli (E^d) for epoxy compositions were determined by measuring longitudinal (C_l) and shear (C_s) wave speeds

$$C_l^2 = \frac{E^d}{\rho}\frac{(1-v)}{(1+v)(1-2v)}, \quad C_s^2 = \frac{E^d}{\rho}\frac{1}{2(1+v)'}, \tag{1}$$

in these compositions using ultrasonic pulse-echo technique. In the above, ρ and v denote apparent density and Poisson's ratio, respectively. The ultrasonic longitudinal and shear wave transducer–receivers having crystal diameter 3 and 5 mm, operating at frequencies of 2.5 and 10 MHz, were used. The measured velocities monotonically decrease with increasing volume fraction, as shown in Fig. 1. The apparent densities of different compositions were evaluated independently and are

Table 1
Material properties

Properties	Microballoons	Epoxy
Mean size	$\sim 60\,\mu m$	—
Wall thickness	$\sim 400\,nm$	—
K_{Ic} (MPa $\sqrt{m}$) (static)	0.7	1.1 ± 0.1
Tensile modulus (MPa) (static)	—	3016
Tensile strength (MPa) (static)	—	58
Density (g/cc)	0.13	1.18
Viscosity (centipoises)	—	213

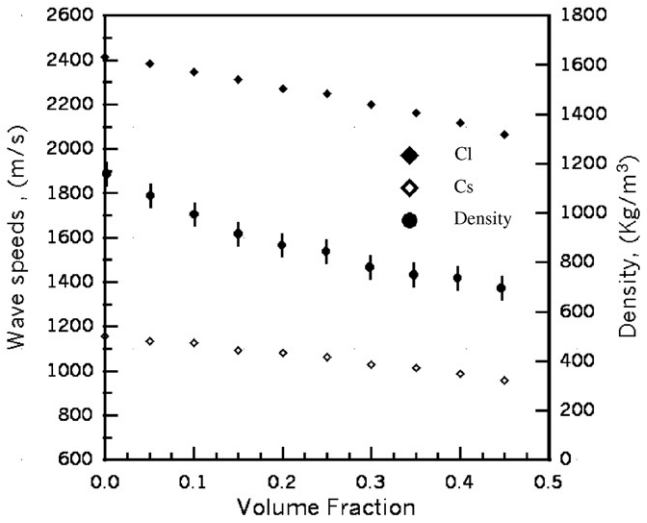

Fig. 1. Longitudinal and shear wave speeds along with density variation for microballoon-dispersed syntactic epoxy compositions.

also shown. The wave speed measurements were used in conjunction with measured densities to determine dynamic Young's modulus and Poisson's ratio. The variation of dynamic Young's modulus with volume fraction of microballoons is shown in Fig. 2. The Young's modulus reduces monotonically with microballoon volume fraction over the entire range. Due to the loading rate dependency of epoxy, measured dynamic value of Young's modulus of unfilled epoxy is higher than the static values listed in Table 1 and compares well with the values reported for this epoxy in the literature [19]. The values of Poisson's ratio in these compositions were found to be nearly constant at 35 ± 0.001.

Next, comparison of the measurements with micromechanics predictions-based Hashin–Shtrikman estimation [20] was carried out. It should be noted that, for spherical filler particles in two-phase compositions, lower bounds are known to accurately predict apparent Young's modulus and hence recommended [21]. For a two-phase mixture comprising of matrix and spherical fillers, the apparent bulk (B) and shear (μ) moduli are expressed in terms of the corresponding properties of the matrix (subscript 'm') and filler (subscript 'f') as

$$B_c = B_f + \frac{V_f}{1/(B_m - B_f) + 3(1 - V_f)/(3B_m + 4B_f)},$$
$$\mu_c = \mu_f + \frac{V_f}{1/(\mu_m - \mu_f) + (6(1 - V_f)(B_m - 2\mu_m)/5\mu_m(3B_m + 4\mu_m))},$$
$$E_c = \frac{9B_c\mu_c}{3B_c + \mu_c}, \tag{2}$$

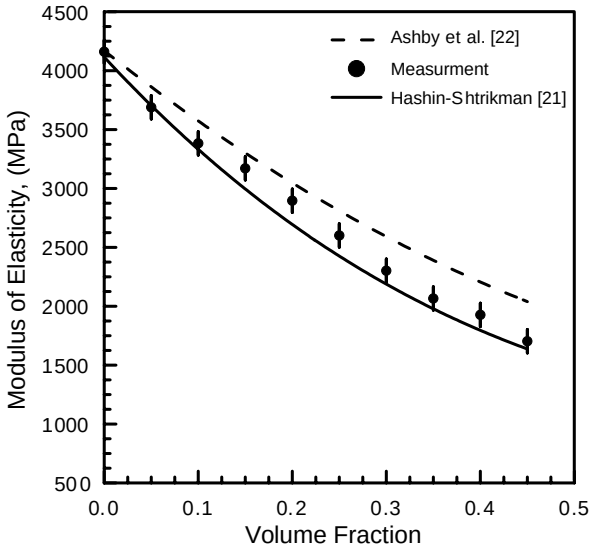

Fig. 2. Comparison between predicted and measured dynamic Young's moduli for microballoon-dispersed syntactic epoxy compositions.

where V_f is the filler volume fraction and subscript 'c' denotes the properties of the composite. The bulk and shear modulus estimates of the porous material in terms of pore volume fraction and properties of the matrix were determined by setting values of B_f and v_f equal to zero. Subsequently, the Young's modulus was determined from the apparent bulk and shear moduli using Eq. (2). The values of Young's modulus thus obtained are shown in Fig. 3. Excellent agreement between the measurements and predictions are clearly evident and reinforcement of the matrix by the filler, if any, is therefore negligible. Also shown in Fig. 2 are the Young's modulus predictions (broken lines) by Gibson and Ashby [22] for cellular solids. The predictions based on this model over estimate the values of E^d in this case.

3. Dynamic crack initiation toughness

The crack initiation toughness or critical stress intensity factors $(K_I)_{cr}$ of microballoon filled epoxy with respect to the pore volume fraction were determined using dynamic impact tests in three-point bending configuration. Edge notched beams with microballoon volume fraction in the range 0–0.45 and dimensions 150 mm × 20 mm × 6 mm were prepared. An initial notch of root radius 75 μm and length 5 mm was made using high-speed circular saw. The notch was subsequently extended into a sharp crack by gently tapping a wedge into the notch mouth, forcing the crack tip to 'pop' and extend by a few millimeters and arrest. Care was exercised to ensure the tip of the wedge from contacting the tip of the notch, thereby preventing undue residual deformations at the crack tip. The samples were subjected

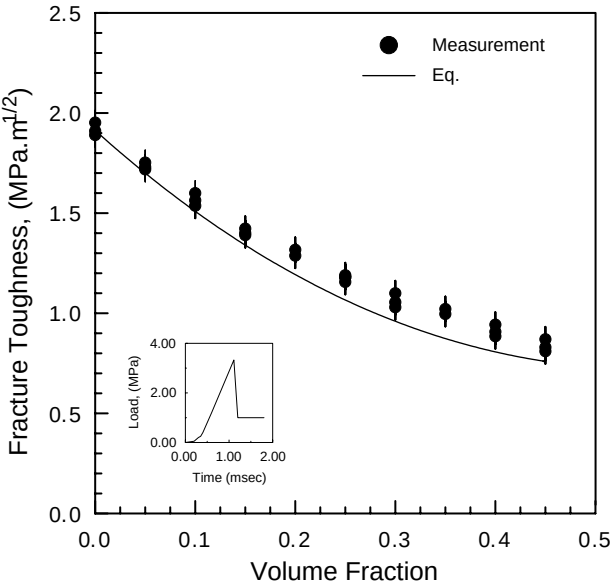

Fig. 3. The variation of dynamic crack initiation toughness of syntactic epoxy foams with microballoon volume fraction.

to impact loading (impact velocity of 1.5 m/s, deadweight 90 N) in an Instron-Dynatup-8210 instrumented drop tower. Integral to the deadweight is a cylindrical tup, with a hemispherical end of radius 12.7 mm, that impacts the specimen directly on the edge opposite to the cracked edge. Load and displacement histories experienced by the tup were recorded by a PC-DAQ system. The maximum load (P_{cr}) registered at the tup was used for determining the dynamic crack initiation toughness using [23]

$$(K_I)_{cr} = Y\frac{P_{cr}S}{BW^{3/2}}, \tag{3}$$

where Y is the geometric factor. In the above, S, B and W are span, thickness and height of the beam samples, respectively. Typically, 4–5 samples were tested for each volume fraction and the failure load in each case was used to determine crack initiation toughness. The apparent critical stress intensity factors, $[(K_I)_{cr}]_c$, determined from the above are plotted as a function of volume fraction of the microballoons in Fig. 3. (The rate of increase in stress intensity factor prior to initiation in all specimens tested was 19 ± 1.8 MPa $\sqrt{\text{m}}$/ms.) The measurements monotonically decrease with increasing volume fraction of the microballoons. This trend is similar to the observation of other investigators for brittle ceramics having different degrees of porosity [24]. The values of $[(K_I)_m]_{cr}$ for unfilled epoxy is approximately 1.9 MPa $\sqrt{\text{m}}$ and compared well with earlier results for this material reported by Rousseau and Tippur [25].

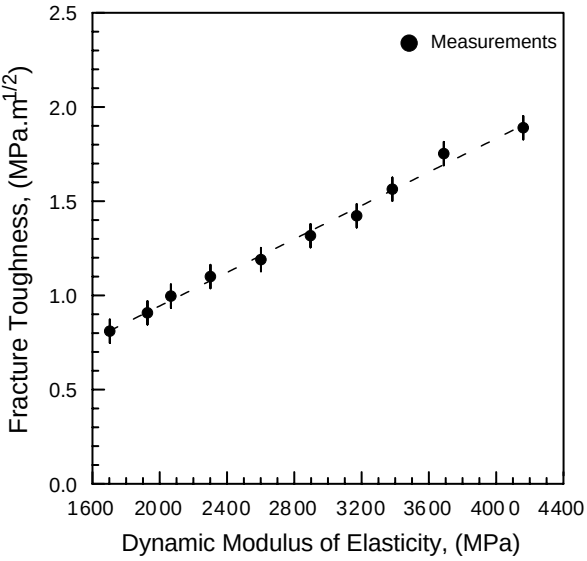

Fig. 4. Linear relationship between dynamic Young's modulus and dynamic stress intensity factor for syntactic epoxy compositions.

Interestingly, the reduction of crack initiation toughness values with microballoon volume fraction has similarities with the variation of Young's modulus (Fig. 2) for the same material compositions. This similarity can be further ascertained by plotting $(K_I)_{cr}$ vs. E^d as shown in Fig. 4. The linear relationship between the two quantities is clearly evident. El-Hadek and Tippur [17] have introduced a simple model to predict critical stress intensity factors for brittle porous materials using linear elastic fracture mechanics considerations along with Hashin–Shtrikman Young's modulus predictions for porous compositions. The model is based on strain energy balance in porous materials, where the apparent strain ε_c in the porous medium is equated to the average matrix strain $\langle \varepsilon_m \rangle$ in the same direction. That is

$$(\varepsilon_c \approx \langle \varepsilon_m \rangle) \Rightarrow \left(\sigma_c \approx \frac{E_c}{E_m} \langle \sigma_m \rangle\right), \tag{4}$$

where σ denotes stress. For uniaxial loading situations, apparent stress in the porous composite can be expressed in terms of the average matrix stress and the Young's modulus ratio of the composite relative to the matrix, as in Eq. (4). Then, the apparent stress intensity factor $(K_I)_c$and hence crack initiation toughness $[(K_I)_{cr}]_c$for a generic mode-I crack in a porous material can be expressed in terms of the average matrix stress $\langle \sigma_m \rangle$, to get

$$\begin{aligned} (K_I)_c &= Y\sigma_c\sqrt{\pi a}, \\ [(K_I)_{cr}]_c &= \frac{E_c}{E_m}(Y\langle \sigma_m \rangle \sqrt{\pi a})_{cr} = \frac{E_c}{E_m}[(K_I)_{cr}]_m, \end{aligned} \tag{5}$$

where a represents generic flaw size, and $[(K_I)_{cr}]_m$ is the crack initiation toughness of the matrix material. Thus, Eq. (5) suggests that $[(K_I)_{cr}]_c$ variation would be similar to that of the Young's modulus of the porous solid since Young's modulus and crack initiation toughness for the matrix are constant. The predicted values (solid line) of $[(K_I^d)_c]_{cr}$ from Eq. (5) for different volume fraction of microballoons are shown in Fig. 3 and excellent agreement between predictions and measurements are evident.

4. Dynamic crack initiation and growth—optical measurements

4.1. Optical method

The optical method of reflection coherent gradient sensing (CGS) [26] was used to collect information related to the out-of-plane crack tip deformations in samples prior to and following crack initiation. A schematic of the optical set-up is shown in Fig. 5. An Argon-ion laser beam ($\lambda = 514\,\text{nm}$) was expanded and collimated to illuminate a circular spot of $\sim 50\,\text{mm}$ diameter on the specimen. The reflected light beam, containing information about the local out-of-plane deformations of the surface from its original state of flatness, was then transmitted through a pair of Ronchi gratings to shear the object wave front laterally perpendicular to the grating lines. All the diffracted wave fronts were then collected by a positive lens and displayed as a linear array of spots on the focal plane, where either the $+1$ or -1 diffraction orders were filtered and imaged. The 'camera', comprising of the positive

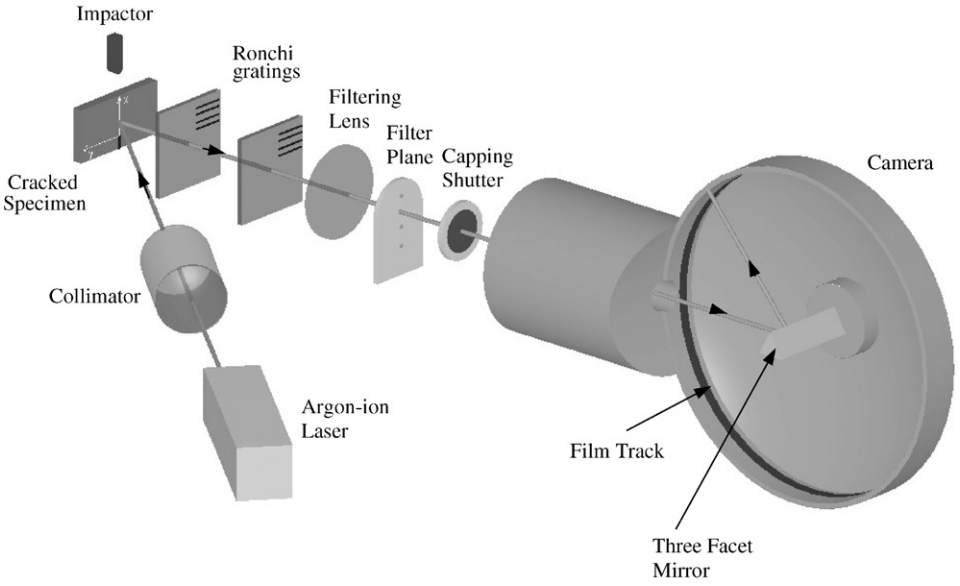

Fig. 5. The schematic of reflection CGS and high-speed photography set-up.

lens and the image plane, was kept focussed on the object surface. The resulting fringes represent surface slopes in the x-direction (along the crack line and perpendicular to the grating lines), and are described by the governing equation of reflection CGS

$$\frac{\partial w}{\partial x} \approx \frac{\delta w}{\delta x} = \frac{Np}{2\Delta}, \quad N = 0, \pm 1, \pm 2, \ldots, \tag{6}$$

where N denotes fringe orders, p is the pitch of the gratings (25 μm), Δ is the grating separation distance (49 mm) and $\delta(\bullet)$ is the difference operator. Assuming plane stress conditions, the out-of-plane displacement w can be related to the in-plane normal stresses and elastic constants as

$$\varepsilon_z \approx \frac{2w}{B} = \frac{-\nu}{E}(\sigma_x + \sigma_y), \tag{7}$$

where B is the thickness of the specimen.

4.2. Experimental set-up

A schematic of the experimental set-up is shown in Fig. 5. The dynamic measurement system consisted of an impactor, pulse laser, CGS interferometer and a continuous access high-speed camera (Beckman–Whitley 339-B). During the experiment, a pneumatically operated impactor with a steel cylindrical head having a hemispherical tip was launched towards the specimen (impact velocity ~ 5.8 m/s). During its descent, the hammer first triggered a photodetector to open the capping shutter located in front of the high-speed camera, allowing light to reach its internal cavity. Soon after that, the specimen was subjected to one point symmetric impact. An adhesive-backed copper tape placed on the top edge of the beam closed an electric circuit when contacted by the hammer. This initiated a string of laser pulses for a total duration corresponding to a single sweep of the laser beam on the film track. The light entering the camera was then reflected-off of a spinning three-facet mirror mounted on a turbine shaft. The reflected light beam was swept on the film held stationary in a film track as discrete images. At the end of that period, the capping shutter was closed avoiding over-writing on the film. In the current experiments, the laser pulse was repeated every 5 μs with a pulse width of 50 ns and a total recording duration of approximately 340 μs. With the settings used, approximately 70 images were written over a 270° angle at a rate of 200,000 frames per second.

4.3. Specimen preparation for optical investigations

Syntactic foam specimens of three select volume fractions of 0.05, 0.25, and 0.45 were prepared for optical measurements. The specimens were machined into 152.4 mm × 43 mm × 8.5 mm slabs. Due to the microstructure of the foam, it was not possible to obtain a specularly reflective surface by directly depositing a thin layer of aluminum on a 152.4 mm × 43 mm face of the sample. Therefore, an optical flat was first coated with a thin layer aluminum film using vacuum deposition technique. This

layer of aluminum was then transferred to the specimen surface using a few drops of epoxy (same as the matrix material of the foam). Once the epoxy was cured the glass disc was pried-off leaving the specimen surface coated with a specularly reflective layer. The thickness of the epoxy-aluminum layer was about 8–12 μm, very small compared to the sample thickness. Next, an 8 mm long single edge notch (root radius ~ 150 μm) was introduced in each specimen using high-speed diamond impregnated circular saw.

4.4. Optical results

Several experiments were carried out with all the three types of homogenous epoxy syntactic foams. An example of the interference fringes obtained for a volume fraction of 0.25 is shown in Fig. 6. For brevity, only selected frames of the entire

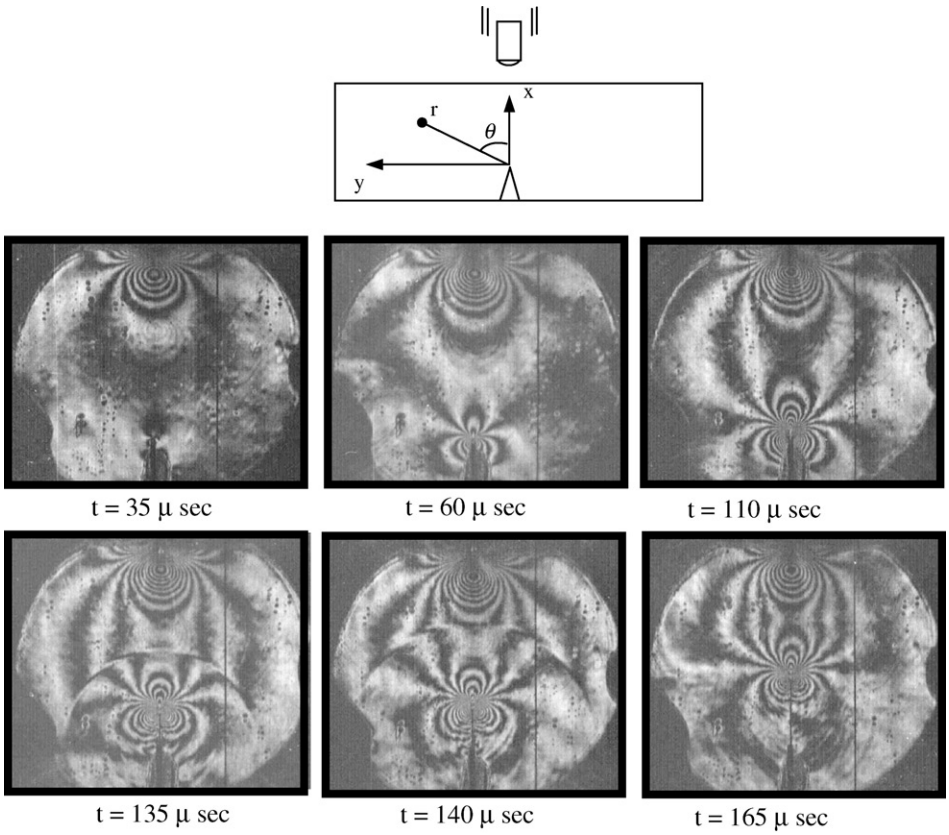

Fig. 6. Representative CGS interferograms representing contours of $\delta w/\delta x$ in a syntactic epoxy foam (volume fraction 0.25) slab impact loaded on edge opposing the crack tip. (The vertical line is at a distance of 10 mm from the crack.) Fringe sensitivity $\sim 0.015^{\circ}$/fringe.

event are shown. The evolution of the fringes, both at the point of impact (top edge) and the crack tip fringes, representing contours of constant $\delta w/\delta x$ can be readily seen. (A line parallel to the crack line on the specimen at a distance of 10 mm is drawn for determining magnification factor of the images.) The frame corresponding to $t = 110\,\mu s$ corresponds to a time (measured from impact) just before crack initiation. In the next two frames shown ($t = 135$ and $140\,\mu s$) a stress wave released from the propagating crack tip can be clearly seen as a circular trace in the interferograms. Based on the two consecutive images, the stress wave speed was found to closely match with that of the Rayleigh wave speed for this material. Additionally, crack tip fringes appear to be the tri-lobed interference patterns with apogee of each set of lobes along $\theta = 0^\circ$, and $\pm 120^\circ$. This is consistent with the fringe patterns anticipated based on mode-I K-dominant description of crack tip deformations [26] for $\delta w/\delta x$.

Optical measurements were used to determine instantaneous crack tip locations. Using forward difference approximation, instantaneous crack speeds (V) were estimated for all the three volume fractions. The crack speed data is presented in Fig. 7. The crack speed is normalized relative to the Rayleigh wave speed C_R of the corresponding material and the time is normalized by the longitudinal wave speed C_l and specimen height W. Evidently, crack initiation occurs earlier in the foam with

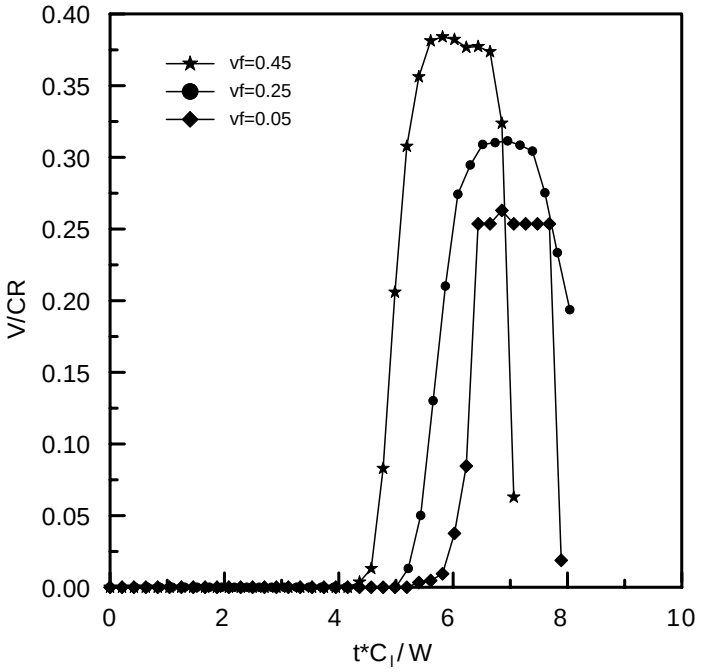

Fig. 7. Variation of normalized crack speed with time after impact for volume fractions 0.05, 0.25 and 0.45.

the highest volume fraction of microballoons, $V_f = 0.45$, followed by the ones with 0.25 and 0.05, respectively. Further, in each case, there is a rapid acceleration of the crack ($\sim 13.3 \times 10^6\,\mathrm{m/s^2}$) following initiation with a nearly constant crack speed attained for a short duration of 30–40 μs before rapid deceleration as the crack encounters reflected stress waves from the specimen boundaries. Another interesting aspect is that the samples with higher volume fraction of microballoons attain higher crack speeds between $0.25C_R$ to nearly $0.4C_R$. (It may be interesting to determine the upper shelf of the crack speeds, which could not be done during the current investigation due to the difficulty in processing foams with higher volume fraction of microballoons.)

4.5. Dynamic stress intensity factors

The fringe patterns for all the three volume fractions of microballoons were analyzed to obtain stress intensity factor histories. This was done using over-deterministic least-squares analysis of the fringes in conjunction with asymptotic crack tip stress fields for a steadily growing crack in a planar homogeneous, isotropic, elastic solid [27]. In doing so, the K-dominant assumptions were relaxed since interference patterns in Fig. 6 suggest interaction between the deformation fields at the impact point and the crack tip location. Explicit expressions for crack tip fields in this case are given by

$$(\sigma_x + \sigma_y) = \sum_{m=1}^{\infty} A_m(t) r_1^{(m/2-1)} \cos\left(\frac{m}{2} - 1\right)\theta_1, \tag{8}$$

where r_1, θ_1 are the scaled crack tip polar coordinates moving with the crack tip, A_m denote the coefficients of the asymptotic expansion with $A_1(t)$ related to the dynamic stress intensity factor as $A_1 = 2f(V)K_I^D/\sqrt{2\pi}$. The velocity function $f(V)$ is given by

$$f(V) = \frac{(1+\alpha_s^2)(\alpha_1^2 - \alpha_s^2)}{4\alpha_s\alpha_s - (1+\alpha_s^2)^2},$$

$$\text{where } \alpha_{s:l} = \sqrt{1 - \left(\frac{V}{C_{l:s}}\right)^2} \quad \text{and} \quad r_1 e^{i\theta_1} = (x + i\alpha_1 y). \tag{9}$$

In the above, $f(V)$ approaches unity as the crack velocity V approaches zero allowing determination of stress intensity factors ($K_I^D(t) = K_I^d(t)$) prior to crack initiation.

Fringes were digitized around the crack tip to obtain fringe order and fringe location data. Based on prior CGS investigations [26], which show that the regions least afflicted by crack tip triaxiality in finite thickness specimens to be $r/B > 0.4$, and $90^\circ < |\theta| < 135^\circ$, the fringes were digitized and used in the analysis. The coefficients $A_m(t)$ were evaluated by minimizing the least-squares error $(\delta w/\delta x - Np/2\Delta)^2$ (w as given in the right-hand side of Eqs. (6)–(9)) at all the digitized data points with respect to the unknown coefficients. The values for instantaneous mode-I stress intensity factors K_I^d or $K_I^D(t)$were determined from $A_1(t)$.

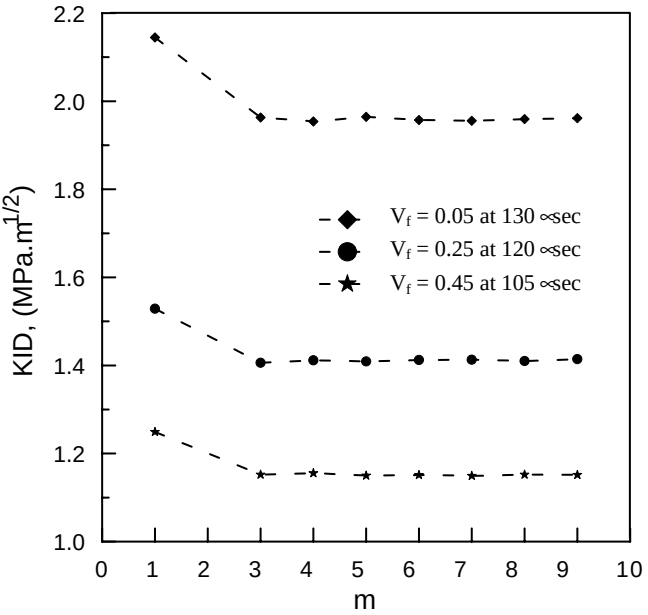

Fig. 8. Variation of dynamic stress intensity factor with the number of terms in the expansion for $(\sigma_x + \sigma_y)$ used in the least-squares analysis.

The need for using higher order terms for evaluating stress intensity factors was first established. Fig. 8 shows variation of stress intensity factor, $K_I^D(t)$, with the number of terms, m, used in the expansion for $(\sigma_x + \sigma_y)$. Analysis for a typical fringe pattern from each experiment is depicted. Evidently, as the number of terms used in the least-squares analysis increase the value of the stress intensity factor drops and attains a plateau. In all cases, value of K_I remains nearly unchanged beyond $m = 3$. It should be noted that $m = 2$ in Eq. (8) corresponds to the so-called T-stress which does not affect the CGS fringes.

The stress intensity factor histories for the three cases obtained are shown in Fig. 9. Crack tip stress intensity factors increase monotonically in each case until crack initiation. The crack initiates at 105, 120 and 130 μs, respectively, for the three volume fractions of 0.05, 0.25 and 0.45, respectively. The rate of increase of stress intensity factors prior to crack initiation (dK_I^d/dt) in nearly constant $(\sim 44 \pm 2\,\text{MPa}\sqrt{\text{m}}/\text{ms})$ in all the three cases. After crack initiation, the values of $K_I^D(t)$ remain nearly constant for a short duration (25–30 μs) before becoming oscillatory as the returning stress waves reflected from the boundaries reach the crack tip. This region of nearly constant $K_I^D(t)$ corresponds to accelerating crack after initiation in each case. The stress intensity factor at initiation is the lowest in case of the foam with a microballoon volume fraction of 0.45 followed by the ones with 0.25 and 0.05, respectively. This is consistent with the drop tower test results reported in Fig. 3. Further, The values of K_I^D at initiation from optical measurement

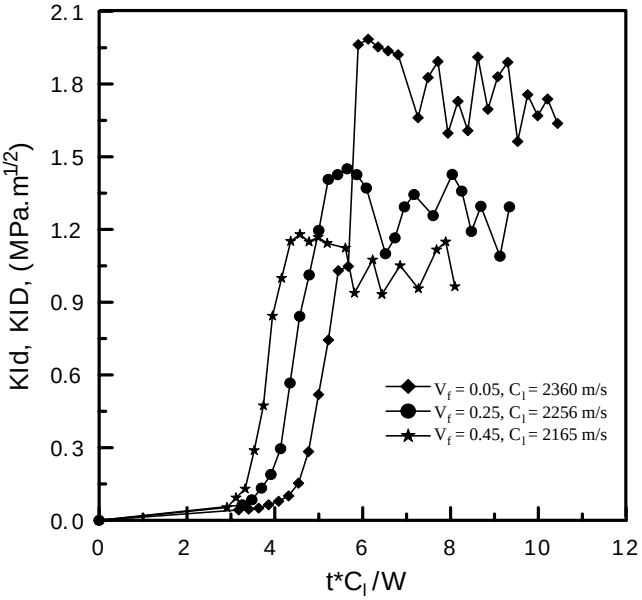

Fig. 9. Mode-I dynamic stress intensity factor histories for three different epoxy syntactic foams.

are slightly higher than their counterparts obtained from the drop tower tests. This is attributed to (a) in the optical tests, the value of dK_I^d/dt is higher ($\sim 44\,\text{MPa}\sqrt{\text{m/ms}}$) than the drop tower tests ($\sim 19\,\text{MPa}\sqrt{\text{m/ms}}$), and (b) specimens used in the optical tests had 150 μm root radius notch instead of a sharp crack as in the drop tower tests.

The velocity dependence of dynamic fracture toughness is widely reported in the literature [28] for polymers and metals. Accordingly, existence of this behavior in all the three cases of syntactic epoxy foams was also examined. In Fig. 10 measured fracture toughness values, K_I^D, are plotted against crack speed (normalized by the respective Rayleigh wave speed). In each case, within the accuracy of measurements, there appears to be no significant crack speed dependence in each of these cases.

Fracture surface of each of three foams was examined using scanning electron microscopy (SEM). To facilitate microscopic observation in this polymeric material, a few Angstroms thick gold layer was sputtered on to a fractured surface. The observations were made at a location where the crack speed in each case is same and equal to the maximum speed in the foam with volume fraction 0.05. The corresponding micrographs are shown in Fig. 11. Evidently, hemispherical fracture of the microballoons is evident in each case. Additionally, there is no wide spread interfacial separation between the microballoons and the matrix. Also evident in the micrographs are non-planar dynamic crack growth involving microbranching of the matrix resulting in a rather rugged of the fractured matrix surface. These contribute to the mechanical behavior of the syntactic foams under consideration comparable to that of truly porous materials.

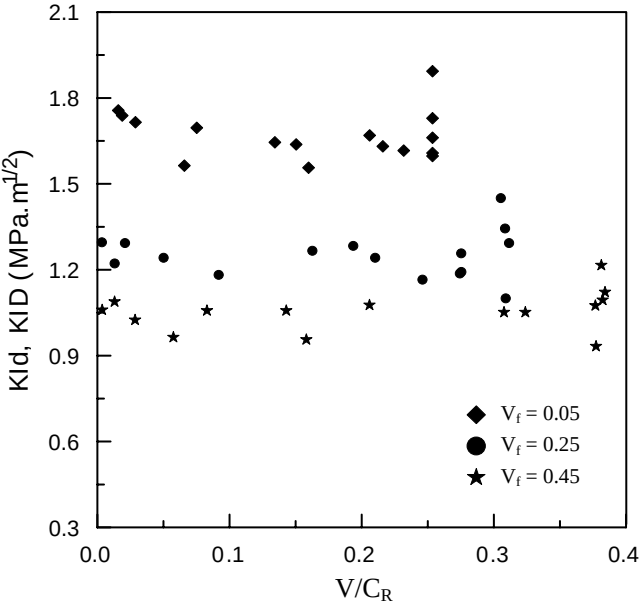

Fig. 10. Dependence of dynamic fracture toughness on crack speed in epoxy syntactic foams.

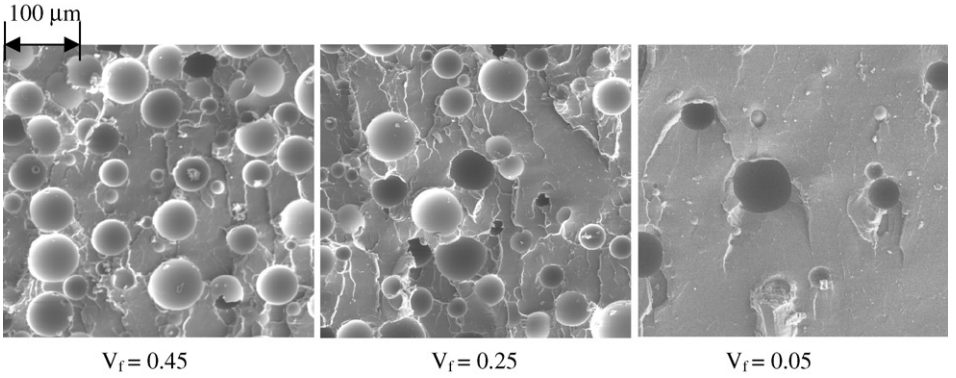

Fig. 11. Scanning electron micrographs of dynamically fractured syntactic foam surfaces. The location of the micrograph corresponds to a region where the apparent crack speed is the same (and equal to the maximum speed in the syntactic foam with volume fraction 0.05).

5. Summary

Dynamic fracture behavior of syntactic epoxy foams with microballoons in the volume fraction range of 0–45% was examined. The foams were made by dispersing microsize ($\sim$60 μm) hollow glass balloons having sub-micron ($\sim$0.4 μm) wall thickness in low-viscosity epoxy matrix. Longitudinal and shear wave speeds of

homogeneous sheet samples of different volume fractions have been measured using ultrasonic pulse-echo measurements. The dynamic Young's modulus and Poisson's ratio for each volume fraction was obtained from wave speed measurements along with density measurements. Monotonically decreasing Young's modulus with increasing volume fraction of microballoons was observed. The measurements were in very good agreement with Hashin–Shtrikman lower-bound predictions for elastic porous solids.

Dynamic crack initiation toughness and crack growth behaviors were determined from instrumented drop-tower tests. Specimens with single edge sharp cracks were subjected to low-velocity (1.5 m/s) impact loading in three-point bending configuration. Using maximum tup load from load-history records, crack initiation toughness for each volume fraction was determined. Measurements show a monotonic reduction in crack initiation toughness with volume fraction and a linear relationship with Young's modulus over the entire range of volume fractions studied. Prediction based on an extended Hashin–Shtrikman model shows good agreement with the measurements. Next, homogeneous samples of three selected volume fractions ($V_f = 0.05$, 0.25 and 0.45) were optically studied using the method of reflection CGS and high-speed photography. Transient crack tip deformations in foam samples subjected to impact loading (impact velocity ~ 5.8 m/s) were measured. Pre- and post-crack initiation events were successfully captured and results indicate higher crack speeds in foams with higher microballoon volume fractions. Further, crack initiation occurs earlier in samples with higher degree of porosity. From the interferograms apparent dynamic stress intensity factor histories were extracted using overdeterministic least-squares analysis and asymptotic crack tip fields for steadily propagating dynamic cracks in homogeneous, isotropic, elastic media. In each case rapid increase of dynamic stress intensity factors ($dK_I^d/dt \sim 44\text{MPa}\sqrt{\text{m}}/\text{ms}$) is seen. Following crack initiation, toughness values remain nearly constant and subsequently become oscillatory about a mean value. Optical tests also indicate that stress intensity factors at crack initiation and dynamic crack growth also decrease with increasing volume fraction of microballoons. Further, dynamic fracture toughness does not show any significant dependence on crack speed in the three volume fractions studied.

Acknowledgements

The support of the research by Army Research Office (Grant DAAD-19-01-1-0414) is gratefully acknowledged. Authors would like to thank assistance of Mr. Mike Maleski and Mr. Josh Hewlett during the course of this research.

References

[1] Erikson R. Foams on the cutting edge. Mech Eng 1999;121(1):27–36.
[2] Burcher R. Concepts in submarine design. NY, Cambridge: University Press, 1994.

[3] Watkins L. Syntactic foam buoyancy for production risers. Houston, TX, USA: LLC Press, 1991.
[4] Shutov FA. Syntactic polymer foams. Adv Polym Sci 1986;73/74:63–123.
[5] Heil C, Dittman D, Ishai O. Composite sandwich construction with syntactic foam core: a practical assessment of post impact damage and residual strength. J Compos 1993;24(5):447–50.
[6] Thomas CR. Syntactic carbon foams. J Mater Sci 1973;12:219–33.
[7] Sternfield A. New types and sources of microspheres can help widen RP markets. Mod Plast Int 1983;12(6):43–5.
[8] Priest N, Van de Vyver F. Trace metals and fluoride in bones and teeth. Boca Raton, FL: CRC Press, 1990.
[9] Denny K. A Biomechanical analysis of the effects of hand weights on the arm-swing while walking and running. Microform. University of Oregon, 1996.
[10] Gibson L, Ashby M, Schajer G, Robertson C. The mechanics of two dimensional cellular materials. Proc R Soc 1982;A382:25–42.
[11] Maiti S, Ashby M, Gibson L. Fracture toughness of brittle cellular solids. Scr Metall 1984;18:213–7.
[12] Hashin Z, Shtrikman SJ. A variational approach to the theory of elastic behavior of polycrystals. Mech Phys Solids 1962;10:343–52.
[13] Weng G. Some elastic properties of reinforced solids, with special reference to isotropic ones containing spherical inclusions. Int J Eng Sci 1984;22(7):845–56.
[14] Krstic V, Erickson W. A model for the porosity dependence of Young's modulus in brittle solids based on crack opening displacement. J Mater Sci 1987;22:2881–6.
[15] Nielsen LJ. Strength and stiffness of porous materials. Am Ceram Soc 1990;73:2684–9.
[16] Rizzi E, Papa E, Corigliano A. Mechanical behavior of a syntactic foam: experiments and modeling. Int J Solids Struct 2000;37:5773–94.
[17] El-Hadek M, Tippur H. Simulation of porosity by microballoon dispersion in epoxy and urethane: mechanical measurements and models. J Materials Sci 2002;37(8):1649–60.
[18] Kin HS, Oh HH. Manufacturing and impact behavior of syntactic foam. J Appl Polym Sci 2000;76:1324–8.
[19] Dowling N. Mechanical behavior of materials. Upper Saddle River: New Jersey, Prentice Hall, 1993.
[20] Hashin Z, Shtrikman SJ. A variational approach to the theory of elastic behavior of multiphase materials. Mech Phys Solids 1963;11:127–40.
[21] Hashin Z. The spherical inclusion with imperfect interface. J Appl Mech 1991;58:444–9.
[22] Gibson L, Ashby M, Schajer G, Robertson C. The mechanics of three dimensional cellular materials. Proc R Soc 1982;A382:43–59.
[23] Tada H, Paris P, Irwin G. The stress analysis of cracks handbook. New York: ASME press, 1998.
[24] Rice R. Porosity of ceramics. New York: Marcel Dekker, 1998.
[25] Rousseau C-E, Tippur HJ. Dynamic fracture of compositionally graded materials with cracks along the elastic gradient. Experiments and analysis. J Mech Mater, 2000, accepted for publication.
[26] Tippur HV, Krishnaswamy S, Rosakis AJ. A coherent gradient sensor for crack tip measurements: analysis and experimental results. Int J Fract 1991;48:193–204.
[27] Freund LB, Clifton RJ. On the uniqueness of plane elastodynamic solution for running cracks. J. Elasticity 1974;4(4):293–9.
[28] Broberg K. Cracks and fracture. Portland, OR: Morgan Kaufmanns, 1999.